Polarization entanglement-enabled quantum holography

Hugo Defienne [✉], Bienvenu Ndagano, Ashley Lyons and Daniele Faccio [✉]

Holography is a cornerstone characterization and imaging technique that can be applied to the full electromagnetic spectrum, from X-rays to radio waves or even particles such as neutrons. The key property in all these holographic approaches is coherence, which is required to extract the phase information through interference with a reference beam. Without this, holography is not possible. Here we introduce a holographic imaging approach that operates on first-order incoherent and unpolarized beams, so that no phase information can be extracted from a classical interference measurement. Instead, the holographic information is encoded in the second-order coherence of entangled states of light. Using spatial-polarization hyper-entangled photon pairs, we remotely reconstruct phase images of complex objects. Information is encoded into the polarization degree of the entangled state, allowing us to image through dynamic phase disorder and even in the presence of strong classical noise, with enhanced spatial resolution compared with classical coherent holographic systems. Beyond imaging, quantum holography quantifies hyper-entanglement distributed over 10^4 modes via a spatially resolved Clauser–Horne–Shimony–Holt inequality measurement, with applications in quantum state characterization.

Holography is an essential tool of modern optics[1] at the origin of many applications for microscopic imaging[2], optical security[3] and data storage[4]. In this respect, holographic interferometry is a widely used technique that exploits optical interference to retrieve the phase component of a classical optical field through intensity measurements. For example, phase-shifting holography[5] uses four intensity images I_θ ($\theta \in \{0, \pi/2, \pi, 3\pi/2\}$) of a reference optical field $ae^{i\theta}$ interfering with an unknown field $be^{i\phi}$ to reconstruct the phase profile

$$\phi = \arg\left[I_0 - I_\pi + i(I_{\pi/2} - I_{3\pi/2})\right] \quad (1)$$

Maintaining optical coherence between interfering fields is therefore essential in all holographic protocols. Mechanical instabilities, random phase disorder and the presence of stray light are examples of phenomena that degrade light coherence and hinder the phase reconstruction process.

Although holography is based on classical interference of light waves, the quantum properties of light have inspired a range of new imaging modalities[6], including interaction-free[7,8] and induced-coherence imaging[9], as well as sensitivity-enhanced[10,11] and super-resolution schemes[12,13]. Non-classical sources of light can also produce holograms[14,15], as has been observed with single photons[16] and photon pairs[17].

In this Article, we introduce and experimentally demonstrate a holographic imaging concept that relies on quantum entanglement to carry the image information. Phase images are encoded in the polarization entanglement of hyper-entangled photons and retrieved through spatial intensity correlation measurements (that is, photon coincidence counting). This quantum holographic scheme has several distinguishing features: (1) it is based on remote interferences between two distant photons, which removes the need for path overlap between the reference and illumination beams; (2) it uses a subspace for encoding/decoding phase information that is robust against dephasing decoherence such as the presence of dynamic random phase disorder on the imaging paths; (3) the reliance on a quantum illumination approach provides immunity to

classical noise, for example stray light falling on the sensor during measurement; (4) spatial entanglement enhances the spatial resolution by a factor 1.84 compared with classical holography.

Finally, we demonstrate the potential of quantum holography beyond imaging, in particular for quantum state characterization, by performing a spatially resolved measurement of the Clauser–Horne–Shimony–Holt (CHSH) inequality to quantify hyper-entanglement in generated quantum states.

The conceptual arrangement of our quantum holographic scheme is illustrated in Fig. 1a. Photon pairs entangled in space and polarization[18] interact with two spatial light modulators ('Alice SLM' and 'Bob SLM') and are then detected by two single-photon imaging devices, for example two distinct areas of an electron-multiplying charge coupled device camera ('Alice EMCCD' and 'Bob EMCCD'). The transverse momentum **k** of the photons is mapped onto separated pixels of the SLMs and re-imaged onto the cameras. Alice and Bob shape and detect photons with the momentum of the negative x component ($k_x < 0$) and positive x component ($k_x > 0$), respectively. The quantum state of the photon pair after the SLMs is thus

$$\sum_{\mathbf{k}} \left[|V\rangle_{\mathbf{k}}|V\rangle_{-\mathbf{k}} + e^{i\Psi(\mathbf{k})}|H\rangle_{\mathbf{k}}|H\rangle_{-\mathbf{k}}\right] \quad (2)$$

where Ψ is a relative phase and $|H\rangle$ and $|V\rangle$ represent the horizontal and vertical polarization states of the photons. For a given momentum **k** ($k_x > 0$), $\Psi(\mathbf{k})$ is the sum of three phase terms: $\Psi_0(\mathbf{k})$, $\theta_A(-\mathbf{k})$ and $\theta_B(\mathbf{k})$. $\Psi_0(\mathbf{k})$ is a static phase distortion produced during the photon generation process[19] that is characterized beforehand (Methods). Phases $\theta_A(-\mathbf{k})$ and $\theta_B(\mathbf{k})$ are actively controlled by Alice and Bob by programming pixels at coordinates $-\mathbf{k}$ and **k** of their SLMs. This is made possible by the use of parallel aligned nematic liquid-crystal SLMs, which enable the manipulation of the horizontal polarization of incoming photons but leave the vertical component unchanged.

Quantum holography

Alice first encodes an image $\theta_A(-\mathbf{k})$ in the phase component of entangled photons by programming her SLM with the corresponding
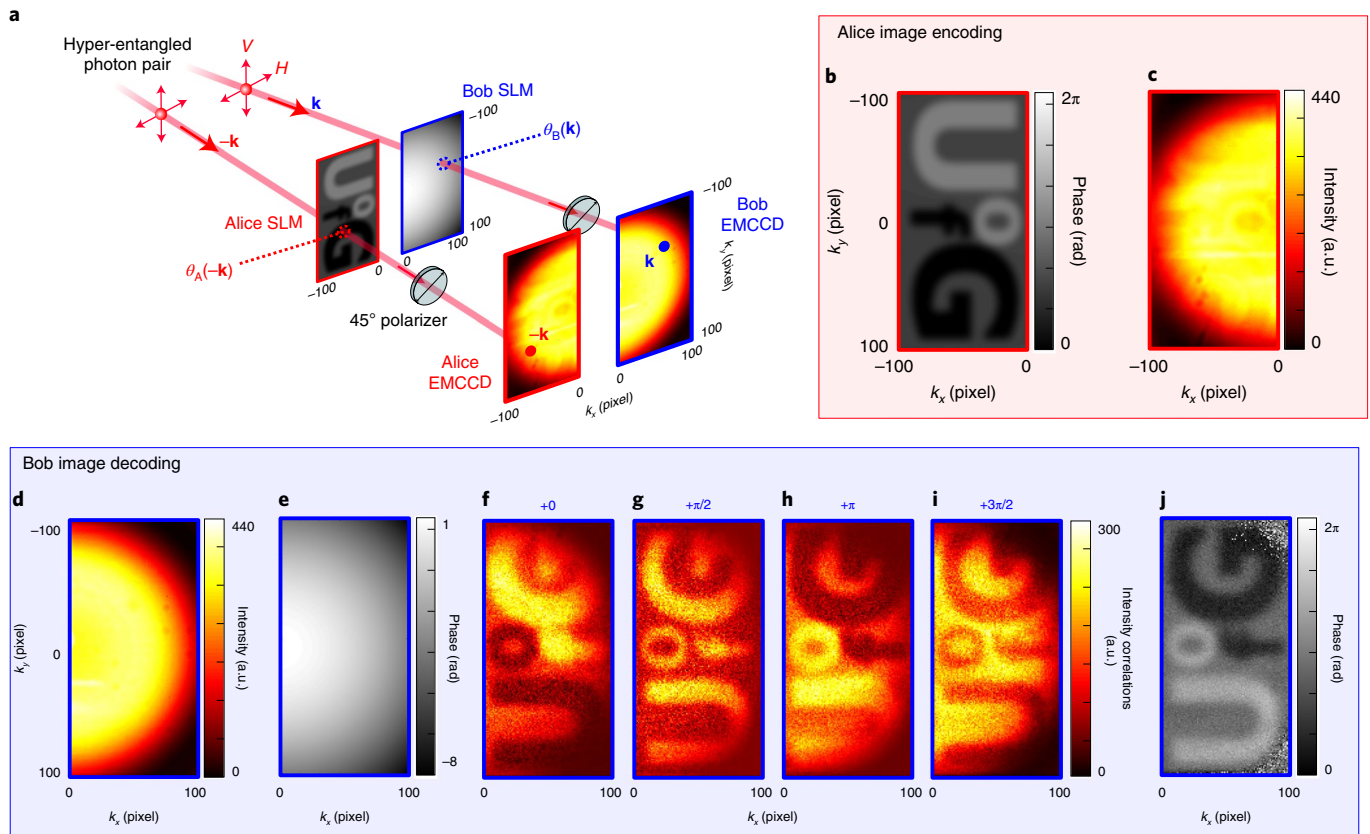
Fig. 1 | Schematic of the quantum holographic reconstruction. a, Space-polarization hyper-entangled photon pairs propagate through two SLMs (Alice SLM and Bob SLM) and are detected by two EMCCD cameras (Alice EMCCD and Bob EMCCD). The transverse momentum **k** of photons with negative x component ($k_x < 0$) are mapped to pixels on Alice's SLM and camera, while those with positive x component ($k_x > 0$) are mapped to pixels on Bob's SLM and camera. Parallel aligned nematic liquid-crystal SLMs allow Alice and Bob to modulate, at any pixel, the horizontal polarization of incoming photons with spatial phases θ_A and θ_B. Two polarizers oriented at 45° are inserted between the SLMs and cameras. **b**, Phase image $\theta_A(-\mathbf{k})$ displayed on Alice SLM. **c,d**, Intensity images measured by Alice (**c**) and Bob (**d**) on their cameras. **e**, The SLM pattern displayed on Bob SLM to compensate for the static phase distortion Ψ_0. **f–i**, Intensity correlation images measured by Bob for different constant phase shifts programmed on Bob SLM: +0 (**f**), +π/2 (**g**), +π (**h**) and +3π/2 (**i**). Each image is obtained by measuring intensity correlations between Bob camera pixels **k** and their symmetric pixels on Alice camera −**k**. **j**, Phase image reconstructed by Bob, with an SNR of over 19 and an n.m.s.e. of 5%. A total of 2.5×10^6 frames were acquired to retrieve the phase at a frame rate of 40 f.p.s., which corresponds to 17 h of acquisition. Intensity and intensity correlation values are in arbitrary units and the same scales are used in all the figures of this Article.

phase pattern. Figure 1b shows the pattern used in our experiments, corresponding to the letters 'UofG'. Bob, on the other hand, displays on his SLM a phase mask $\theta_B(\mathbf{k}) = -\Psi_0(\mathbf{k})$ to compensate for the phase distortion Ψ_0 (Fig. 1e). This correcting phase remains superimposed on all phase masks that Bob programs throughout the experiment. As a result, the phase of the quantum state after the SLMs equals exactly the encoded image $\Psi(\mathbf{k}) = \theta_A(-\mathbf{k})$. In the example shown in Fig. 1b, pixels associated with the letters 'U' and 'o' are encoded as the states $|VV\rangle + |HH\rangle$ ($\Psi = 0$), while 'f' and 'G' are encoded as $|VV\rangle - |HH\rangle$ ($\Psi = \pi$). After programming Alice's phase, we observe that the intensity images measured by both Alice and Bob, shown in Fig. 1c,d, are homogeneous and do not reveal the phase-encoded image. This observation remains valid when including polarizers in front of the cameras, in any orientation.

In the holographic reconstruction step of the process, Bob decodes the image by performing intensity correlation measurements between pixels at **k** of his camera and symmetric pixels at −**k** on Alice's camera[20], with the two polarizers oriented at 45°. This measurement is repeated four times for four different constant phase shifts θ applied on Bob's SLM, resulting in intensity correlation image $R_\theta(\mathbf{k}) \propto 1 + \cos(\theta_A(\mathbf{k}) + \theta)$ (Methods). The phase image programmed on Alice's SLM must remain stationary during

the full process, which takes up to several hours. Figure 1f–i shows four intensity correlation images measured for $\theta \in \{0, \pi/2, \pi, 3\pi/2\}$, which partially reveal the hidden phase. Following a similar approach to classical holography, Bob then reconstructs the encoded image by using equation (1) after replacing I_θ by R_θ. As shown in Fig. 1j, the retrieved image is 180° rotated and is of high quality, with a signal-to-noise ratio (SNR) of over 19 and a normalized mean square error (n.m.s.e.) of 5%. Although the SNR measures the intrinsic quality of the image retrieved by Bob in terms of noise level, the n.m.s.e. quantifies its resemblance to the original image encoded by Alice (Methods). Note that the combination of a highly multimode quantum state with a camera-based multipixel coincidence counting approach removes the need for operating raster-scanning approaches, as used for example in NOON-state microscopy[12].

The photon-pair spatial correlations provide the high-dimensional image space[21], while polarization entanglement carries the grey-scale information at each pixel. The presence of polarization entanglement is therefore essential to this scheme. For example, Fig. 2 shows the results of quantum holography performed with the same encoded image as in Fig. 1a, but using a source of photon pairs that are entangled in space but not in polarization
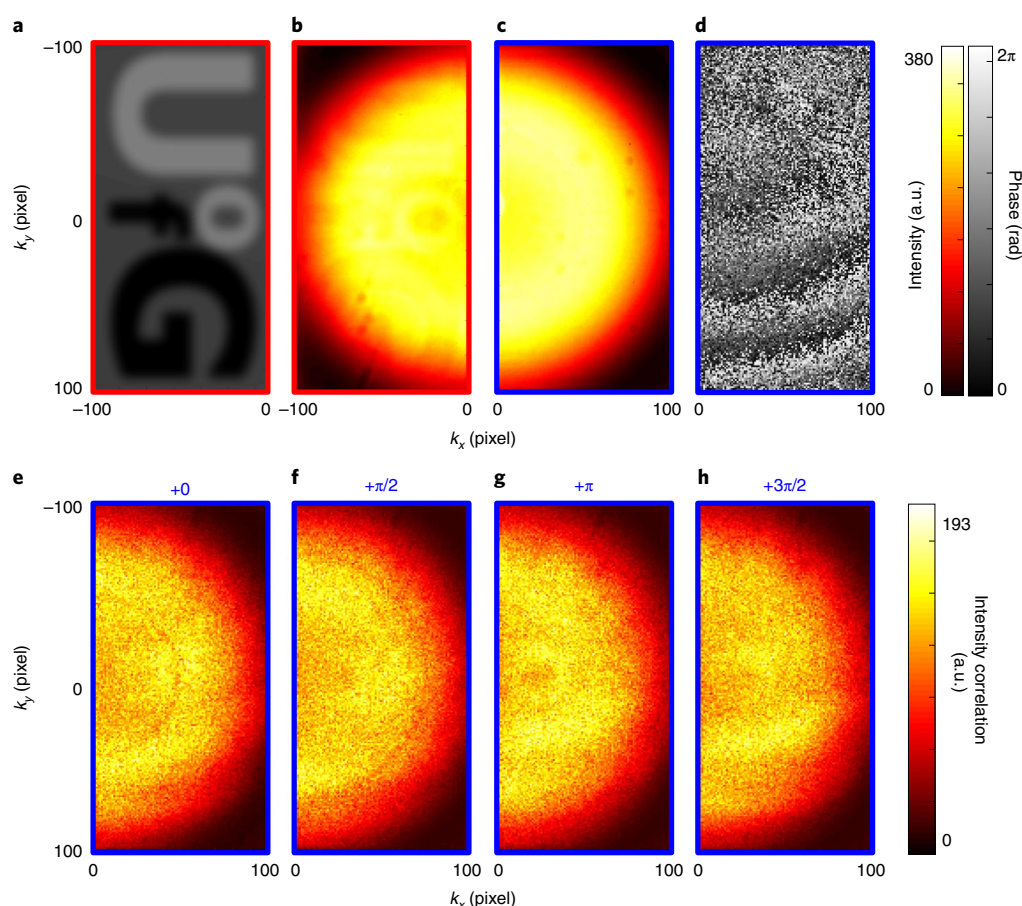
Fig. 2 | Quantum holography without polarization entanglement. a, Phase image encoded by Alice. **b,c**, Intensity images measured by Alice (**b**) and Bob (**c**). **d**, Phase reconstructed by Bob, which does not reveal the encoded image (n.m.s.e. = 95%). **f–i**, Intensity correlation images used in the phase reconstruction process measured for different phase shifts: +0 (**f**), +π/2 (**g**), +π (**h**) and +3π/2 (**i**). A total of 2.5×10⁶ frames were acquired.

(Methods). As in the previous case, intensity images measured by Alice and Bob in Fig. 2b,c do not reveal information about the encoded phase. However, Fig. 2e–h shows that the intensity correlation images acquired during the phase-shifting process do not reveal any image information either, and the phase image cannot be retrieved (n.m.s.e. = 95%), as shown in Fig. 2d. Non-zero values in the intensity correlation images also confirm that (classical) correlations between photon polarizations are present without entanglement; the existence of a phase Ψ is conditioned on the coherence between the two-qubit terms $|VV\rangle$ and $|HH\rangle$ (ref. [22]), and thus on the entanglement in the state. This conclusion only concerns polarization entanglement, because the presence of spatial entanglement is itself not strictly required in our holographic protocol. Therefore, one may design an experimental scheme using photons entangled in polarization but only classically correlated in space to achieve similar results, even if this would be technically much more difficult than using hyper-entangled photons, with no real additional benefits.

Robust subspaces and phase disorder

Here, the phase information is encoded and decoded from a subspace spanned by the two basis states $|H\rangle_{\mathbf{k}}|H\rangle_{-\mathbf{k}}$ and $|V\rangle_{\mathbf{k}}|V\rangle_{-\mathbf{k}}$. We verify, in our quantum holography concept, that the use of this subspace protects the encoded phase information against dephasing decoherence generated by dynamic random phase disorders. Such robustness is linked to the notion of decoherence-free subspaces (DFSs), which have been shown to protect quantum states

against decoherence by exploiting symmetries in system–environment interactions[23]. Figure 3 describes an experimental apparatus in which space-polarization entangled photons propagate through two thin diffusers (Fig. 3, inset) positioned on a motorized translation stage in the image plane of both the SLMs and cameras. In this configuration, the polarization qubits at spatial mode $\mathbf{k}$ undergo the transformations $|V\rangle_{\mathbf{k}} \rightarrow e^{i\Phi(\mathbf{k})}|V\rangle_{\mathbf{k}}$ and $|H\rangle_{\mathbf{k}} \rightarrow e^{i\Phi(\mathbf{k})}|H\rangle_{\mathbf{k}}$, where $\Phi(\mathbf{k}) = \Phi_H(\mathbf{k}) = \Phi_V(\mathbf{k})$ are the identical (because the phase disorder is non-polarization-sensitive) time-varying random phase shifts in spatial mode $\mathbf{k}$ added on the horizontal and vertical polarizations. The dynamic phase term Φ therefore factorizes out and leaves the encoded phase Ψ intact:

$$\sum_{\mathbf{k}} e^{i[\Phi(\mathbf{k})+\Phi(-\mathbf{k})]}\left[|V\rangle_{\mathbf{k}}|V\rangle_{-\mathbf{k}} + e^{i\Psi(\mathbf{k})}|H\rangle_{\mathbf{k}}|H\rangle_{-\mathbf{k}}\right] \quad (3)$$

Figure 4 shows the experimental reconstruction of a phase image via the dynamic phase disorders. Intensity images measured by Alice and Bob are shown in Fig. 4b and 4c, respectively, and the image encoded by Alice (Fig. 4a) is very accurately reconstructed by Bob in Fig. 4d (SNR = 21 and n.m.s.e. = 2%). Phase reconstruction is also achieved through static phase disorder (Supplementary Information), confirming that such robustness does not originate from an averaging effect. Note that all entangled polarization basis sets are robust in the presence of the generic random phase disorder considered here. The equivalent classical states encoded in the basis set $\{|H\rangle_{\mathbf{k}}, |V\rangle_{-\mathbf{k}}\}$ would totally decohere under the same
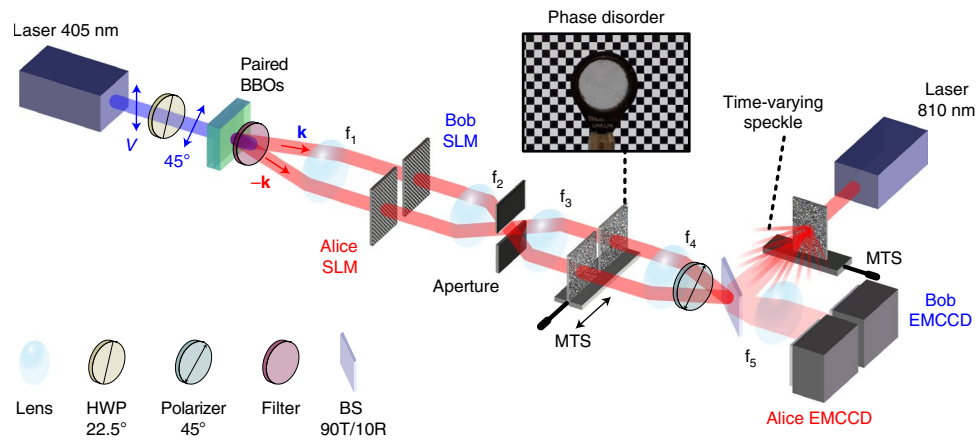
Fig. 3 | Experimental set-up. Light emitted by a laser diode at 405 nm and polarized at 45° illuminates a pair of β-barium borate (BBO) crystals (0.5 mm thickness each) whose optical axes are perpendicular to each other to produce pairs of photons entangled in space and polarization by type I spontaneous parametric downconversion. After the crystals, pump photons are filtered out by a combination of long-pass and band-pass filters. The momentum of red photons is mapped onto an SLM divided into two parts (Alice SLM and Bob SLM) by Fourier imaging with lens f_1. Lenses f_2–f_3 image the SLM plane onto two thin diffusers (inset) positioned on a motorized translation stage (MTS) and lenses f_4–f_5 image it on an EMCCD camera split into two parts (Alice EMCCD and Bob EMCCD); that is, each photon of a pair experiences a phase disorder independent of that experienced by its twin. A polarizer at 45° is positioned between lenses f_4 and f_5. Stray light is inserted by illuminating another dynamic diffuser with a laser (810 nm) to produce a time-varying speckle pattern that is superimposed on top of quantum light using an unbalanced beamsplitter (BS 90T/10R). An adjustable aperture is positioned in the Fourier plane of the SLMs. For clarity, only two propagation paths of entangled photons at **k** and −**k** are represented, although they have a higher-dimensional spatial structure. SLMs, EMCCD cameras and diffusers are represented by pairs, although they are in practice single devices spatially divided into two independent parts. The SLM is represented in transmission, although it operates in reflection. See Methods for further information. HWP, half-wave plate.
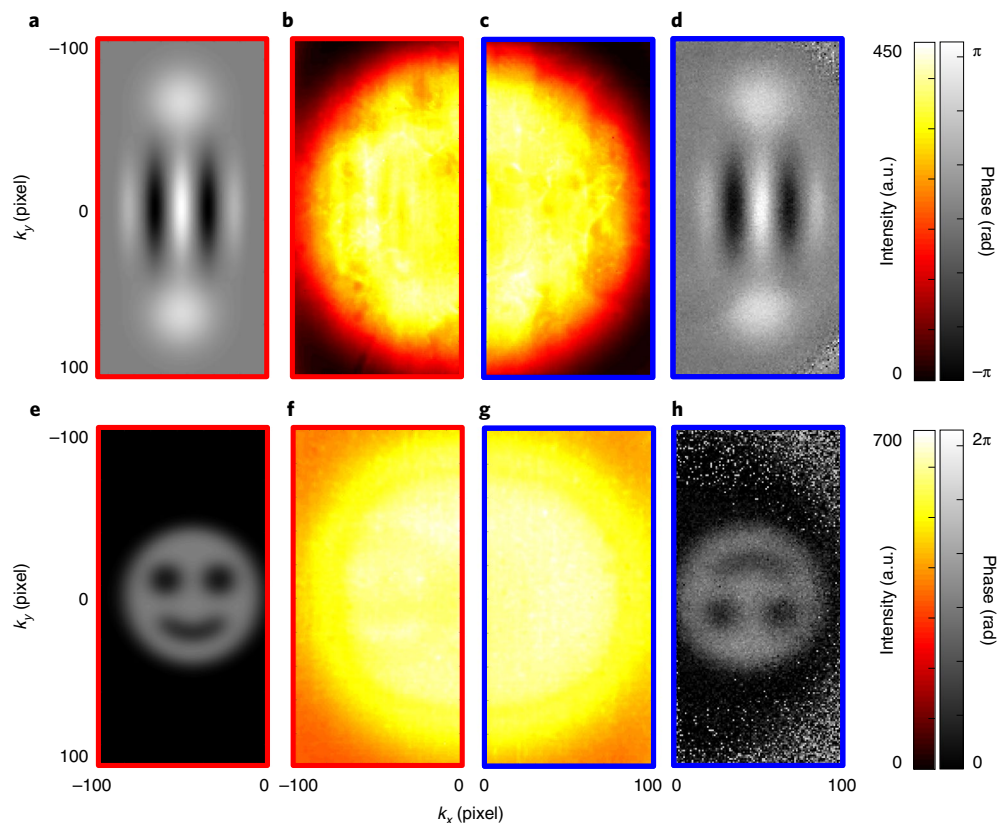
Fig. 4 | Quantum holography through dynamic phase disorder and in the presence of stray light. a, Phase image encoded by Alice. **b,c**, Intensity images measured by Alice (**b**) and Bob (**c**) through dynamic phase disorder. **d**, Phase image reconstructed by Bob through dynamic phase disorder, with SNR = 21 and n.m.s.e. = 2%. **e**, Phase image programmed by Alice. **f,g**, Intensity images measured by Alice (**f**) and Bob (**g**) in the presence of dynamic stray light with an average classical/quantum intensity ratio of 0.5. **h**, Phase image reconstructed by Bob in the presence of dynamic stray light with SNR = 9 and n.m.s.e. = 17%. All images were reconstructed from 5×10^6 frames.
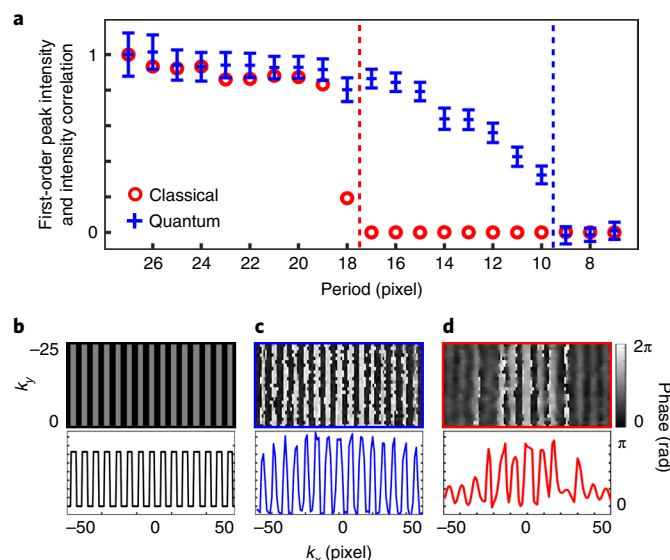
Fig. 5 | Resolution enhancement. a, Intensity (red circles, classical light) and intensity correlation values (blue crosses, quantum light) of first-order diffraction peaks measured for different grating periods in the presence of the aperture using the classical and quantum holographic systems, respectively. The cutoff periods are 17.5 ± 0.5 pixels (classical) and 9.5 ± 0.5 pixels (quantum). **b**, 0–π phase grating with 16-pixel-period encoded by Alice (zoom of 25 × 100 pixels). **c**,**d**, Phase images of a 16-pixel-period phase grating reconstructed using classical (**d**) and quantum (**c**) holographic systems (zoom of 25 × 100 pixels), respectively. Corresponding projections along the k_x axis (black, red and blue curves) are shown below the images. A total of 5 × 10⁶ frames were acquired for each case under quantum illumination. In **a**, the error bars for the red points are too small to be shown on the graph. The error bars of the blue points represent the standard deviations of the noise in the first-order diffraction peaks.

conditions. One may also show that our state is robust against other forms of decoherence with different symmetries, such as collective dephasing decoherence[24], but that are less realistic in our experimental arrangement. These results show that the use of specific subspaces to encode information, as previously shown with DFSs for implementing robust quantum information-processing protocols[25–28], can also be useful in the context of imaging for reconstructing polarization-sensitive phase objects through optical disorder. Although certain classical common-path interferometers may achieve similar robustness, we underline that this is impossible in any classical non-common-path interferometers because the presence of uncorrelated phase disorders in different arms would completely erase the classical phase information. Here, instead, the coherence between the two interferometer arms, and thus the encoded phase, is preserved thanks to the presence of polarization entanglement.

Quantum illumination and dynamic stray light
We have shown (for example, in Fig. 1) that phase information is reconstructed from a quantum illumination (QI) approach that relies on four intensity correlation images obtained by coincidence counting[29,30]. QI protocols use spatial correlation between photons to achieve enhanced imaging in the presence of noise, as recently demonstrated for amplitude objects illuminated by entangled pairs corrupted by static stray light[31,32]. Here, we exploit this robustness to image polarization-sensitive phase objects in the presence of dynamic stray light falling on both Alice and Bob sensors. Seen from the context of the QI proposal by Lloyd[29], the photon from the entangled pair detected by Bob plays the role of the 'ancilla',

while its twin detected by Alice probes the object. As shown in Fig. 3, a time-varying speckle pattern is superimposed onto the Alice and Bob sensors. This addition of classical light is clearly visible in the intensity images in Fig. 4f,g. Because photons emitted by the classical source are not spatially correlated, they are not detected by the intensity correlation measurements used for quantum phase reconstruction. Therefore, a phase image encoded by Alice (Fig. 4e) is accurately retrieved by Bob in the presence of dynamic classical stray light (Fig. 4h), with only a lower SNR compared to the case without stray light. Importantly, the SNR reduction does not indicate a permanent loss of image information content and can always be compensated by acquiring more frames (see Supplementary Information for a quantitative analysis of the variation of SNR with quantum–classical intensity ratio and number of frames).

Entanglement and spatial resolution
Resolution enhancement using entangled photon pairs has been theorized[33] and exploited in scanning-based imaging approaches[34,35]. This effect lies in the foundations of optical coherence, precisely reflecting the difference between its first- and second-order degrees[36]. We demonstrate it here in the context of full-field quantum holographic imaging, using a classical coherent holographic imaging system for comparison (details are provided in the Methods). We insert an aperture in the Fourier plane of the SLMs (Fig. 3) to control the transmitted spatial frequencies, then image this plane onto the camera by replacing lens f₅ by a lens of half-focal length (single-lens imaging). Phase grating objects with different periods are then programmed onto Alice SLM. When using classical holography, we observe (Fig. 5a) that the intensity of the first-order diffraction peak vanishes for grating periods below 17.5 ± 0.5 pixels. Conversely, using our quantum holographic system, the first-order diffraction peak of the intensity correlation diffraction pattern only disappears for a shorter period of 9.5 ± 0.5 pixels (Methods and Extended Data Fig. 1). The difference in frequency cutoff between the two systems corresponds to an enhancement of the spatial resolution by a factor of 1.84 ± 0.05 (ref. [37]), close to the maximum theoretical value of 2 (ref. [33]). The resolution enhancement effect is also observed using the imaging configuration (with lens f₅): a 16-pixel-period phase grating can be near perfectly resolved using our quantum holographic approach (Fig. 5c), while a significant degradation is observed when using classical holography (Fig. 5d).

Hyper-entanglement characterization in high dimensions
By harnessing the fundamental link between quantum state tomography and second-order optical coherence holography, the quantum holography scheme enables characterization of hyper-entanglement in high dimensions. Indeed, the measurements performed by Bob in the phase-stepping holographic process correspond to projections in the diagonal ($\theta_B \in \{0, \pi\}$) and circular ($\theta_B \in \{\pi/2, 3\pi/2\}$) polarization basis (Fig. 6a). Similarly, Alice can use her SLM to perform measurements in the corresponding rotated basis $\theta_A \in \{\pi/4, 3\pi/4, 5\pi/4, 7\pi/4\}$ (see also Extended Data Fig. 2). During this process, the use of a compensation phase mask programmed on Bob SLM (Fig. 1e) is important to ensure optimal orientation of the measurement bases. As shown in Fig. 5b, these measurement settings provide spatially resolved measurements of the CHSH inequality across 10,789 pairs of pixels. Taking into account the finite momentum correlation width of the photons, $\sigma_k = [1.326 \pm 0.001] \times 10^3$ rad m⁻¹ (~1.1 pixel), one may conclude that Alice and Bob share up to 8,900 polarization-entangled states in parallel. Furthermore, an additional measurement in the position space of the photons enables to measure their position correlation width, $\sigma_r = 10.85 \pm 0.06$ μm (refs. [38,39]). One can then also verify the presence of spatial entanglement in the quantum state through an Einstein–Podolsky–Rosen (EPR) type inequality[21], which in our case results in $\sigma_r \sigma_k = [1.44 \pm 0.01] \times 10^{-2} < \frac{1}{2}$ (Methods).
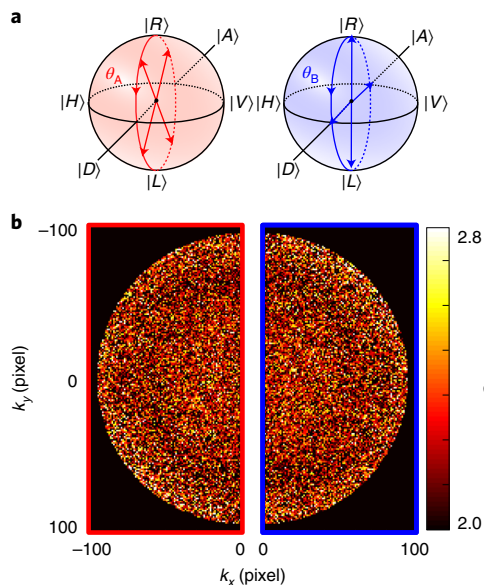
Fig. 6 | Spatially resolved CHSH inequality violation. a, Poincaré spheres representing the projections performed by Alice and Bob with their SLMs. $|D\rangle$ and $|A\rangle$ are two eigenstates of the diagonal polarization basis and $|R\rangle$ and $|L\rangle$ are the two eigenstates of the circular polarization basis. Bob performs measurements directly in the diagonal and circular basis, while Alice operates in a similar basis rotated by $\pi/4$. **b**, Values of the CHSH correlation coefficient S measured at different pairs of pixels of Alice's and Bob's sensors within two half-disks containing 14,129 pairs of pixel. The two half-disks correspond to areas where the direct intensity is non-null and homogeneous. Images are calculated from the intensity correlation measured for 16 combinations of angles θ_A and θ_B (Extended Data Fig. 2). The CHSH inequality is violated ($S > 2$) in 10,789 of the 14,129 pairs of pixels. An average value of $\langle S \rangle = 2.20 \pm 0.003 > 2$ is obtained by averaging S values over the full two half-disk areas. See Methods for further details.

Application potential

Our quantum holography concept can also be applied to the imaging of real-world objects, aside from the phase patterns imprinted on the SLM shown so far. As an example, in Extended Data Fig. 3 we show phase images obtained by removing the SLM and passing the entangled photons through bird feathers and adhesive tape. In biology, our scheme can be useful for measuring small variations of birefringence in biological structures for investigating cell pathophysiology[40] and tissue damage[41] and for ophthalmologic preclinical diagnosis[42,43], typical situations in which classical holographic techniques can be limited by the presence of specimen-induced phase distortions (that is, phase disorder) and stray light that cannot be blocked. Furthermore, combining our approach with concepts from differential interference contrast imaging[44] enables to extend its range of applications to non-polarization-sensitive phase objects, with the potential for large field-of-view imaging microscopy[45]. An illustration of such an extended set-up is shown in Extended Data Fig. 4, together with experimental results of quantum phase imaging of non-birefringent silicone oil droplets. Beyond the optical domain, our approach could also be extended to other imaging methods such as electron-based techniques[46], with potential for investigating complex biological systems at low radiation and with further enhanced resolution.

Quantum states entangled in high dimensions and multiple degrees of freedom are also promising for moving beyond the limitations of current quantum communication and information-processing technologies[47–50]. One of the central challenges is ascertaining the presence of entanglement in a given

quantum state, however complex and large it may be. In this respect, our quantum holography concept can be used for characterizing entanglement in both space and polarization distributed across up to 10^4 modes, a task that would be prohibitively time-consuming (if not impossible) using raster-scanning and single-outcome projective measurement techniques[51,52].

Conclusions

In summary, we have shown that it is possible to perform holography without (first-order) coherence, a concept that is not possible in classical physics and broadens the remit of what is achievable with holography. Holographic imaging is enabled by quantum entanglement, which does not rely on classical optical coherence. Information about the image is encoded in the relative phases between the polarization-entangled two-photon qubit states (that is, phase Ψ in $|VV\rangle + e^{i\Psi}|HH\rangle$) and is distributed over the transverse spatial dimension through the high-dimensional structure of spatial entanglement. By harnessing the physical concepts linked to the notion of entanglement, including QI and DFS, it is possible to achieve resolution-enhanced measurement of polarization-sensitive phase objects through random phase disorder and stray light, with practical advantages over classical holography. Furthermore, there is a fundamental correspondence between quantum holography and quantum tomography that extends the concept to quantum state characterization, including the analysis of hyper-entangled states in high dimensions. One current practical limitation of our quantum holographic protocol is its long acquisition time (on the order of several hours) resulting from the low frame rate of EMCCD cameras. However, thanks to the rapid development of faster and cheaper sensors for imaging quantum correlations[53,54], we expect quantum holography to move towards practical applications for biological imaging and sensing, and also for characterizing complex high-dimensional quantum states, which are likely to be at the heart of tomorrow's quantum optical communications and information-processing technologies.

Online content

Any methods, additional references, Nature Research reporting summaries, source data, extended data, supplementary information, acknowledgements, peer review information; details of author contributions and competing interests; and statements of data and code availability are available at https://doi.org/10.1038/s41567-020-01156-1.

References

1. Gabor, D. A new microscopic principle. *Nature* **161**, 777–778 (1948).
2. Marquet, P. et al. Digital holographic microscopy: a noninvasive contrast imaging technique allowing quantitative visualization of living cells with subwavelength axial accuracy. *Opt. Lett.* **30**, 468–470 (2005).
3. Refregier, P. & Javidi, B. Optical image encryption based on input plane and Fourier plane random encoding. *Opt. Lett.* **20**, 767–769 (1995).
4. Heanue, J. F., Bashaw, M. C. & Hesselink, L. Volume holographic storage and retrieval of digital data. *Science* **265**, 749–752 (1994).
5. Yamaguchi, I. & Zhang, T. Phase-shifting digital holography. *Opt. Lett.* **22**, 1268–1270 (1997).
6. Moreau, P.-A., Toninelli, E., Gregory, T. & Padgett, M. J. Imaging with quantum states of light. *Nat. Rev. Phys.* **1**, 367–380 (2019).
7. White, A. G., Mitchell, J. R., Nairz, O. & Kwiat, P. G. 'Interaction-free' imaging. *Phys. Rev. A* **58**, 605–613 (1998).
8. Pittman, T. B., Shih, Y. H., Strekalov, D. V. & Sergienko, A. V. Optical imaging by means of two-photon quantum entanglement. *Phys. Rev. A* **52**, R3429–R3432 (1995).
9. Lemos, G. B. et al. Quantum imaging with undetected photons. *Nature* **512**, 409–412 (2014).
10. Nasr, M. B., Saleh, B. E. A., Sergienko, A. V. & Teich, M. C. Demonstration of dispersion-canceled quantum-optical coherence tomography. *Phys. Rev. Lett.* **91**, 083601 (2003).

11. Brida, G., Genovese, M. & Berchera, I. R. Experimental realization of sub-shot-noise quantum imaging. *Nat. Photon.* **4**, 227–230 (2010).
12. Ono, T., Okamoto, R. & Takeuchi, S. An entanglement-enhanced microscope. *Nat. Commun.* **4**, 2426 (2013).
13. Tenne, R. et al. Super-resolution enhancement by quantum image scanning microscopy. *Nat. Photon* **13**, 116–122 (2019).
14. Abouraddy, A. F., Saleh, B. E. A., Sergienko, A. V. & Teich, M. C. Quantum holography. *Opt. Express* **9**, 498–505 (2001).
15. Asban, S., Dorfman, K. E. & Mukamel, S. Quantum phase-sensitive diffraction and imaging using entangled photons. *Proc. Natl Acad. Sci. USA* **116**, 11673–11678 (2019).
16. Chrapkiewicz, R., Jachura, M., Banaszek, K. & Wasilewski, W. Hologram of a single photon. *Nat. Photon.* **10**, 576–579 (2016).
17. Devaux, F., Mosset, A., Bassignot, F. & Lantz, E. Quantum holography with biphotons of high Schmidt number. *Phys. Rev. A* **99**, 033854 (2019).
18. Barreiro, J. T., Langford, N. K., Peters, N. A. & Kwiat, P. G. Generation of hyperentangled photon pairs. *Phys. Rev. Lett.* **95**, 260501 (2005).
19. Hegazy, S. F. & Obayya, S. S. A. Tunable spatial–spectral phase compensation of type-I (ooe) hyperentangled photons. *J. Opt. Soc. Am. B* **32**, 445–450 (2015).
20. Defienne, H., Reichert, M. & Fleischer, J. W. General model of photon-pair detection with an image sensor. *Phys. Rev. Lett.* **120**, 203604 (2018).
21. Howell, J. C., Bennink, R. S., Bentley, S. J. & Boyd, R. W. Realization of the Einstein–Podolsky–Rosen paradox using momentum- and position-entangled photons from spontaneous parametric down conversion. *Phys. Rev. Lett.* **92**, 210403 (2004).
22. Kwiat, P. G., Barraza-Lopez, S., Stefanov, A. & Gisin, N. Experimental entanglement distillation and 'hidden' non-locality. *Nature* **409**, 1014–1017 (2001).
23. Lidar, D. A. & Birgitta Whaley, K. in *Irreversible Quantum Dynamics* (eds Benatti, F. & Floreanini, R.) 83–120 (Lecture Notes in Physics, Springer, 2003).
24. Kwiat, P. G., Berglund, A. J., Altepeter, J. B. & White, A. G. Experimental verification of decoherence-free subspaces. *Science* **290**, 498–501 (2000).
25. Kielpinski, D. et al. A decoherence-free quantum memory using trapped ions. *Science* **291**, 1013–1015 (2001).
26. Viola, L. et al. Experimental realization of noiseless subsystems for quantum information processing. *Science* **293**, 2059–2063 (2001).
27. Yamamoto, T., Hayashi, K., Özdemir, S. K., Koashi, M. & Imoto, N. Robust photonic entanglement distribution by state-independent encoding onto decoherence-free subspace. *Nat. Photon.* **2**, 488–491 (2008).
28. Banaszek, K., Dragan, A., Wasilewski, W. & Radzewicz, C. Experimental demonstration of entanglement-enhanced classical communication over a quantum channel with correlated noise. *Phys. Rev. Lett.* **92**, 257901 (2004).
29. Lloyd, S. Enhanced sensitivity of photodetection via quantum illumination. *Science* **321**, 1463–1465 (2008).
30. Tan, S.-H. et al. Quantum illumination with Gaussian states. *Phys. Rev. Lett.* **101**, 253601 (2008).
31. Defienne, H., Reichert, M., Fleischer, J. W. & Faccio, D. Quantum image distillation. *Sci. Adv.* **5**, eaax0307 (2019).
32. Gregory, T., Moreau, P.-A., Toninelli, E. & Padgett, M. J. Imaging through noise with quantum illumination. *Sci. Adv.* **6**, eaay2652 (2020).
33. Giovannetti, V., Lloyd, S., Maccone, L. & Shapiro, J. H. Sub-Rayleigh-diffraction-bound quantum imaging. *Phys. Rev. A* **79**, 013827 (2009).
34. Boto, A. N. et al. Quantum interferometric optical lithography: exploiting entanglement to beat the diffraction limit. *Phys. Rev. Lett.* **85**, 2733–2736 (2000).
35. Mitchell, M. W., Lundeen, J. S. & Steinberg, A. M. Super-resolving phase measurements with a multiphoton entangled state. *Nature* **429**, 161–164 (2004).
36. Glauber, R. J. The quantum theory of optical coherence. *Phys. Rev.* **130**, 2529 (1963).
37. Goodman, J. W. *Introduction to Fourier Optics* (Roberts and Company Publishers, 2005).
38. Moreau, P.-A., Mougin-Sisini, J., Devaux, F. & Lantz, E. Realization of the purely spatial Einstein–Podolsky–Rosen paradox in full-field images of spontaneous parametric down-conversion. *Phys. Rev. A* **86**, 010101 (2012).
39. Edgar, M. P. et al. Imaging high-dimensional spatial entanglement with a camera. *Nat. Commun.* **3**, 984 (2012).
40. Lee, K. et al. Quantitative phase imaging techniques for the study of cell pathophysiology: from principles to applications. *Sensors* **13**, 4170–4191 (2013).
41. Wang, J., Dong, L., Chen, H. & Huang, S. Birefringence measurement of biological tissue based on polarization-sensitive digital holographic microscopy. *Appl. Phys. B* **124**, 240 (2018).
42. Pircher, M. et al. Imaging of polarization properties of human retina in vivo with phase resolved transversal PS-OCT. *Opt. Express* **12**, 5940–5951 (2004).
43. Götzinger, E., Pircher, M., Sticker, M., Fercher, A. F. & Hitzenberger, C. K. Measurement and imaging of birefringent properties of the human cornea with phase-resolved, polarization-sensitive optical coherence tomography. *J. Biomed. Opt.* **9**, 94–103 (2004).
44. Allen, R. D. & David, G. B. The Zeiss–Nomarski differential interference equipment for transmitted-light microscopy. *Z. Wissen. Mikrosk. Mikroskop. Tech.* **69**, 193–221 (1969).
45. Terborg, R. A., Pello, J., Mannelli, I., Torres, J. P. & Pruneri, V. Ultrasensitive interferometric on-chip microscopy of transparent objects. *Sci. Adv.* **2**, e1600077 (2016).
46. Madan, I. et al. Holographic imaging of electromagnetic fields via electron–light quantum interference. *Sci. Adv.* **5**, eaav8358 (2019).
47. Erhard, M., Krenn, M. & Zeilinger, A. Advances in high-dimensional quantum entanglement. *Nat. Rev. Phys.* **2**, 365–381 (2020).
48. Barreiro, J. T., Wei, T.-C. & Kwiat, P. G. Beating the channel capacity limit for linear photonic superdense coding. *Nat. Phys.* **4**, 282–286 (2008).
49. Graham, T. M., Bernstein, H. J., Wei, T.-C., Junge, M. & Kwiat, P. G. Superdense teleportation using hyperentangled photons. *Nat. Commun.* **6**, 7185 (2015).
50. Deng, F.-G., Ren, B.-C. & Li, X.-H. Quantum hyperentanglement and its applications in quantum information processing. *Sci. Bull.* **62**, 46–68 (2017).
51. Barbieri, M., Cinelli, C., Mataloni, P. & De Martini, F. Polarization-momentum hyperentangled states: realization and characterization. *Phys. Rev. A* **72**, 052110 (2005).
52. Krenn, M. et al. Generation and confirmation of a (100×100)-dimensional entangled quantum system. *Proc. Natl Acad. Sci. USA* **111**, 6243–6247 (2014).
53. Lubin, G. et al. Quantum correlation measurement with single photon avalanche diode arrays. *Opt. Express* **27**, 32863–32882 (2019).
54. Ndagano, B. et al. Imaging and certifying high-dimensional entanglement with a single-photon avalanche diode camera. *npj Quantum Inf.* **6**, 94 (2020).

Methods

Experimental layout. A paired set of β-barium borate (BBO) crystals with dimensions of $0.5 \times 5 \times 5$ mm each were cut for type I spontaneous parametric downconversion at 405 nm. In our set-up, these were optically contacted with one crystal rotated by 90° about the axis normal to the incidence face. Both crystals were rotated slightly around the horizontal and vertical axes to ensure near-collinear phase matching of photons at the output (the rings collapsed into disks). The pump was a continuous-wave laser operating at 405 nm (Coherent OBIS-LX) with an output power of ~200 mW and a beam diameter of 0.8 ± 0.1 mm. A 650-nm-cutoff long-pass filter was used to block pump photons after the crystals, together with a band-pass filter centred at 810 ± 5 nm. The SLM was a phase-only modulator (Holoeye Pluto-2-NIR-015) with $1,920 \times 1,080$ pixels and a pixel pitch of 8 µm. The camera was an EMCCD (Andor Ixon Ultra 897) that operates at −60 °C, with a horizontal pixel shift readout rate of 17 MHz, a vertical pixel shift every 0.3 µs, a vertical clock amplitude voltage of +4 V above the factory setting and an amplification gain set to 1,000. This had a pixel pitch of 16 µm. The exposure time was set to 3 ms. The camera speed was ~40 f.p.s. for a region of interest of 200×200 pixels, allowing retrieval of a phase image with SNR ≈ 20 in ~17 h (that is, 2.5×10^6 frames in total). Characterization of our system showed that the camera detected ~0.1 pairs per spatial mode per second. The detection efficiency of the entire set-up was ~0.48. The classical source was a superluminescent diode laser (Qphotonics) with a spectrum of 810 ± 15 nm that was filtered using a band-pass filter at 810 ± 5 nm to match the photon pair's spectrum. Lens f_1 was composed of a series of three lenses with focal lengths of 45 mm, 125 mm and 150 mm positioned in a Fourier imaging configuration where the distance between each pair of lenses equalled the sum of the focal lengths of each lens. The whole system can be seen as a lens f_1 with an effective focal length of $f_1 = 54$ mm. The focal lengths of the other lenses are $f_2 = 150$ mm, $f_3 = f_4 = 75$ mm, $f_5 = 100$ mm and $f_6 = 175$ mm. The distances between components were as follows: crystal plane to lens f_1, 54 mm; lens f_1 to SLMs, 54 mm; SLMs to lens f_2, 150 mm; lens f_2 to aperture, 150 mm; aperture to lens f_3, 75 mm; lens f_3 to phase disorder, 75 mm; phase disorder to lens f_4, 75 mm; lens f_4 to beamsplitter, 75 mm; beamsplitter to lens f_5, 100 mm; lens f_5 to camera, 100 mm. The magnification factor from the SLM plane to the camera plane was 0.7. The diffuser was a plastic sleeve layer with thickness of <100 µm, roughness of 46 µm and a decorrelation time of 183 ms. Supplementary Sections 6 and 9 provide further details on the diffuser properties and the quantum source.

Intensity correlation images. The camera sensor was split into two identical regions of interest composed of 201×101 pixels associated with Alice and Bob, respectively. To measure intensity correlations, the camera first acquires a set of N images. Values of intensity correlation $R(\mathbf{k})$ between a pixel at $\mathbf{k}$ on Bob's side and the symmetric pixel at $-\mathbf{k}$ on Alice's side are then calculated by subtracting the product of the intensity values measured in the same frame by the product of the intensity values measured in successive frames, and averaging over all the frames:

$$R(\mathbf{k}) = \frac{1}{N}\sum_{l=1}^{N}[I_l(\mathbf{k})I_l(-\mathbf{k}) - I_l(\mathbf{k})I_{l+1}(-\mathbf{k})] \qquad (4)$$

where I_l denotes the lth frame[20]. Supplementary Section 1 provides further details on the intensity correlation measurement.

Quantum holography. Intensity correlation measurements performed between pixels $\mathbf{k}$ and $-\mathbf{k}$ with two polarizers oriented at 45° positioned in front of the cameras can be associated with the following measurement operator:

$$\frac{1}{2}[|H\rangle\langle H| + |V\rangle\langle V| + |H\rangle\langle V| + |V\rangle\langle H|]_{\mathbf{k}} \\ \otimes [|H\rangle\langle H| + |V\rangle\langle V| + |H\rangle\langle V| + |V\rangle\langle H|]_{-\mathbf{k}} \qquad (5)$$

For a given pair of pixels $(-\mathbf{k}, \mathbf{k})$, the expectation value of this operator in the state described by equation (2) is

$$R(\mathbf{k}) = \frac{1}{2}[1 + \cos(\Psi(\mathbf{k}))] \qquad (6)$$

During the holographic process, Alice encodes a phase $\theta_A(-\mathbf{k})$ and Bob applies a phase shift θ superimposed over the phase compensation pattern $-\Psi_0(\mathbf{k})$. As a result, intensity correlation measurements performed by Bob for a given θ are given by $R_\theta(\mathbf{k}) = \frac{1}{2}[1 + \cos(\theta_A(\mathbf{k}) + \theta)]$. As in classical holography (equation (1)), Bob then reconstructs the phase image $\theta_A(\mathbf{k})$ image using four successive measurements: $\theta_A(\mathbf{k}) = \arg[R_0(\mathbf{k}) - R_\pi(\mathbf{k}) + i(R_{\pi/2}(\mathbf{k}) - R_{3\pi/2}(\mathbf{k}))]$. Note that, to take into account a more general case, the state in equation (2) can be rewritten as

$$\sum_{\mathbf{k}}\left[e^{i\Psi(\mathbf{k})}|H\rangle_{\mathbf{k}}|H\rangle_{-\mathbf{k}} + \alpha|V\rangle_{\mathbf{k}}|V\rangle_{-\mathbf{k}}\right] \qquad (7)$$

with $\alpha \in [0,1]$. In this case, the expectation value of the operator in equation (5) changes to $\frac{1}{2}[1 + \alpha^2 \cos(\Psi(\mathbf{k}))]$, but $\theta_A(\mathbf{k})$ is still retrieved using equation (1) (albeit with visibility equal to α^2).

Characterization of spatial entanglement. Spatial entanglement in the photon source is characterized by performing intensity correlation measurements between

the positions and momentum of photons, using the method described in refs. [38,39]. Correlation width measurements return values of $\sigma_r = 10.85 \pm 0.06$ µm for position and $\sigma_k = [1.326 \pm 0.001] \times 10^3$ rad m^{-1} for momentum. These values show violation the EPR criterion $\sigma_r \sigma_k = [1.44 \pm 0.01] \times 10^{-2} < \frac{1}{2}$ (ref. [21]). Supplementary Section 2 provides further details, including the correlation images in position and momentum spaces used to estimate the correlation widths.

Phase distortion characterization. The phase distortion $\Psi_0(\mathbf{k})$ originates from the birefringence of the paired BBO crystals used to generate photon pairs[19]. $\Psi_0(\mathbf{k})$ is measured beforehand by performing a holographic measurement between a flat phase pattern programmed on Alice SLM and successive phase shifts displayed on Bob SLM. This characterization process results in a phase distortion of the form $\Psi_0(k_x, k_y) = 4.69k_x^2 + 5.04k_y^2 + 0.02$. In our experiment, a correcting phase mask is directly programmed on Bob SLM to compensate for the phase distortion (Fig. 1e). For holographic imaging of phase objects, we note that, in principle, it would be possible to replace Bob SLM by a rotating polarizer positioned in front of the camera and compensate for the phase distortion afterwards in a post-processing step on a computer. However, the use of a correcting pattern directly implemented on Bob's SLM is important for performing the spatially resolved CHSH measurement (Fig. 6) because it ensures an optimal orientation of the measurement bases. Supplementary Section 4 provides further details on the phase distortion characterization.

SNR, n.m.s.e. and spatial resolution. The SNR is obtained by calculating an averaged value of the phase in a region of the retrieved image where it is constant, and then dividing it by the standard deviation of the noise in the same region. To have a common reference, SNR values are calculated using areas where the phase is constant and equals π. For a fixed exposure time and pump power, the SNR varies as $\sqrt{N}$, where N is the number of images used to reconstruct the intensity correlation images[55]. In the presence of stray light, the SNR decreases as $1/\langle I_d \rangle$, where $\langle I_d \rangle$ is the average intensity of classical light falling on the sensor[31,32]. Quantitative analyses of SNR variation with the number of frames and the intensity of stray light are provided in Supplementary Sections 3 and 7.

The n.m.s.e.[56] quantifies the resemblance between an image reconstructed by Bob and the ground-truth image encoded by Alice. The n.m.s.e. is calculated using the formula

$$\text{n.m.s.e.} = \frac{M_0}{M_\infty} \qquad (8)$$

where M_0 is the mean square error (m.s.e.) measured between the ground truth and the retrieved image and M_∞ is an average value of m.s.e. measured between the ground truth and a set of images composed of phase values randomly distributed between 0 and 2π. The m.s.e. between two images composed of P pixels with values denoted respectively $\{x_i\}_{i\in[[1,P]]}$ and $\{y_j\}_{j\in[[1,P]]}$ is defined as $M = 1/P \sum_{i=1}^{P} |x_i - y_i|^2$. Values of n.m.s.e. range between 1 (retrieved image is a random phase image) and 0 (retrieved image is exactly the ground truth). The spatial resolution in the retrieved image is determined by the spatial correlation width of entangled photons. In our experiment, its value is estimated as $d = 45 \pm 3$ µm, which corresponds to ~3 camera pixels. Supplementary Section 3 provides further details on the spatial resolution characterization.

Photons without polarization entanglement. The results shown in Fig. 2 are obtained using a quantum state defined by the following density operator:

$$\frac{1}{2}\sum_{\mathbf{k}}[|H\rangle_{\mathbf{k}}|H\rangle_{-\mathbf{k}}\langle H|_{\mathbf{k}}\langle H|_{-\mathbf{k}} + |V\rangle_{\mathbf{k}}|V\rangle_{-\mathbf{k}}\langle V|_{\mathbf{k}}\langle V|_{-\mathbf{k}}] \qquad (9)$$

Experimentally, it is produced by switching the polarization of the pump laser between vertical and horizontal polarizations, which is equivalent of using an unpolarized pump. Because entanglement originates fundamentally from a transfer of coherence properties between the pump and the downconverted fields in spontaneous parametric downconversion[57–59], the lack of coherence in the pump polarization induces the absence of polarization entanglement in the produced two-photon state, while spatial and temporal entanglements are maintained[22]. Supplementary Section 5 provides further details on state entanglement in space, but not in polarization.

Reference classical holographic system. The experimental results shown in Fig. 5 were obtained using a holographic system that is a classical version of our quantum protocol, namely a polarization phase-shifting common-path holographic interferometer[60]. In this classical system, a collimated laser beam (810 nm) polarized at 45° illuminates Alice SLM, on which a phase object is programmed (Bob SLM is not used). Alice SLM is imaged onto a single EMCCD camera using the same imaging system as the one described in Fig. 3. Phase-shifting holography is then performed by superimposing four constant phase patterns $(0, \pi/2, \pi, 3\pi/2)$ on top of the programmed phase object and measuring the four corresponding intensity images on the camera. Finally, the phase object is reconstructed using equation (1). Supplementary Section 8 provides more details.

Resolution enhancement measurement. A comparison of the spatial resolution between quantum and classical holographic systems is performed by measuring

their respective frequency cutoff[57]. The results shown in Fig. 5 are obtained by replacing lens f_s in Fig. 3 by a lens with half-focal length ($f_s/2 = 50$ mm) to directly image the Fourier plane of the SLM onto the EMCCD camera. The aperture is also placed in this Fourier plane. In the classical case, measurements are performed by illuminating Alice SLM with a 45° collimated laser beam (see previous section). When programming a phase grating on the SLM, intensity images measured by the EMCCD show a diffraction pattern with three main components: a central zero-order peak and two symmetrically positioned plus or minus first-order peaks. Red circles in Fig. 5a correspond to the intensity of the (plus) first-order peak measured for different grating periods. Because of the aperture, a sharp cutoff is observed at period of 17.5 ± 0.5 pixels. In the quantum case, diffraction patterns are revealed by measuring intensity correlations with the EMCCD camera (that is, second-order coherence)[15,17]. More precisely, a complete intensity correlation matrix $R(\mathbf{r}_1, \mathbf{r}_2)$ is measured for each phase grating using a generalized version of equation (4)[20]:

$$R(\mathbf{r}_1, \mathbf{r}_2) = \frac{1}{N} \sum_{l=1}^{N} [I_l(\mathbf{r}_1)I_l(\mathbf{r}_2) - I_l(\mathbf{r}_1)I_{l+1}(\mathbf{r}_2)] \quad (10)$$

where N is the number of acquired frames, $\mathbf{r}_1$ and $\mathbf{r}_2$ are spatial positions in the Fourier plane (that is, camera pixel positions). Then, the intensity correlation matrix is projected along the minus-coordinate axis $\delta\mathbf{r} = \mathbf{r}_1 - \mathbf{r}_2$ using the formula

$$P(\delta\mathbf{r}) = \sum_{\mathbf{r}} R(\mathbf{r}, \mathbf{r} - \delta\mathbf{r}) \quad (11)$$

where the summation is performed over all illuminated pixels $\mathbf{r}$. The use of such projection to reveal diffraction patterns under quantum illumination was demonstrated in refs. [17,61]. Similarly to the classical case, three peaks of intensity correlations are observed when visualizing intensity correlation in the minus-coordinate basis (diffraction patterns are shown in Extended Data Fig. 1). Blue crosses in Fig. 5a correspond to the intensity of the (plus) first-order peak measured for different grating periods. In this case, a cutoff is observed at a period of 9.5 ± 0.5 pixels, which corresponds to a resolution enhancement of $17.5/9.5 = 1.84 \pm 0.05$. Supplementary Section 8 provides further details on the resolution characterization, including detailed experimental schemes and images of classical and quantum diffraction patterns.

CHSH measurement. A set of 16 intensity correlations images R_{θ_A, θ_B} is first measured using all combinations of uniform phases $\theta_A \in \{\pi/4, 3\pi/4, 5\pi/4, 7\pi/4\}$ and $\theta_B \in \{0, \pi/2, \pi, 3\pi/2\}$ programmed on Alice and Bob SLMs. Then, a correlation image E_{θ_A, θ_B} is calculated using the following formula[62]:

$$E_{\theta_A, \theta_B} = \frac{R_{\theta_A, \theta_B} - R_{\theta_A, \theta_B+\pi} - R_{\theta_A+\pi, \theta_B} + R_{\theta_A+\pi, \theta_B+\pi}}{R_{\theta_A, \theta_B} + R_{\theta_A, \theta_B+\pi} + R_{\theta_A+\pi, \theta_B} + R_{\theta_A+\pi, \theta_B+\pi}} \quad (12)$$

Finally, the image of S values shown in Fig. 6b is obtained using the following equation:

$$S = |E_{\pi/2, \pi/4} - E_{\pi/2, 5\pi/4}| + |E_{0, \pi/4} + E_{0, 5\pi/4}| \quad (13)$$

As shown in Fig. 6, 10,789 pairs of S values measured between Alice and Bob correlated pixels show violation of CHSH inequality $S > 2$, over the total of 14,129 pair of pixels forming the two half-disks. A spatial averaged value of $\langle S \rangle = 2.20 \pm 0.003 > 2$ is estimated by calculating the mean and variance of S values over these 14,129 pairs of pixels. Supplementary Section 2 provides further details on the CHSH measurement, and Extended Data Fig. 2 shows all 16 measured correlation images R_{θ_A, θ_B}.

Data availability

References
55. Reichert, M., Defienne, H. & Fleischer, J. W. Optimizing the signal-to-noise ratio of biphoton distribution measurements. *Phys. Rev. A* **98**, 013841 (2018).
56. Gonzalez, R. C. & Wintz, P. *Digital Image Processing (Applied Mathematics and Computation)* (Addison-Wesley, 1977).
57. Jha, A. K. & Boyd, R. W. Spatial two-photon coherence of the entangled field produced by down-conversion using a partially spatially coherent pump beam. *Phys. Rev. A* **81**, 013828 (2010).
58. Kulkarni, G., Subrahmanyam, V. & Jha, A. K. Intrinsic upper bound on two-qubit polarization entanglement predetermined by pump polarization correlations in parametric down-conversion. *Phys. Rev. A* **93**, 063842 (2016).
59. Kulkarni, G., Kumar, P. & Jha, A. K. Transfer of temporal coherence in parametric down-conversion. *J. Opt. Soc. Am. B* **34**, 1637–1643 (2017).
60. Mukhopadhyay, S., Sarkar, S., Bhattacharya, K. & Hazra, L. Polarization phase shifting interferometric technique for phase calibration of a reflective phase spatial light modulator. *Opt. Eng.* **52**, 035602 (2013).
61. Defienne, H., Reichert, M. & Fleischer, J. W. Adaptive quantum optics with spatially entangled photon pairs. *Phys. Rev. Lett.* **121**, 233601 (2018).
62. Clauser, J. F., Horne, M. A., Shimony, A. & Holt, R. A. Proposed experiment to test local hidden-variable theories. *Phys. Rev. Lett.* **23**, 880–884 (1969).

Acknowledgements

Author contributions
H.D. conceived the original idea, designed and performed the experiment, and analysed the data. H.D., A.L., B.N. and D.F. contributed to the interpretation of the results and manuscript. H.D. prepared the manuscript. D.F. supervised the project.

Competing interests
The authors declare no competing interests.

Additional information
Extended data is available for this paper at https://doi.org/10.1038/s41567-020-01156-1.

Supplementary information is available for this paper at https://doi.org/10.1038/s41567-020-01156-1.

Correspondence and requests for materials should be addressed to H.D. or D.F.
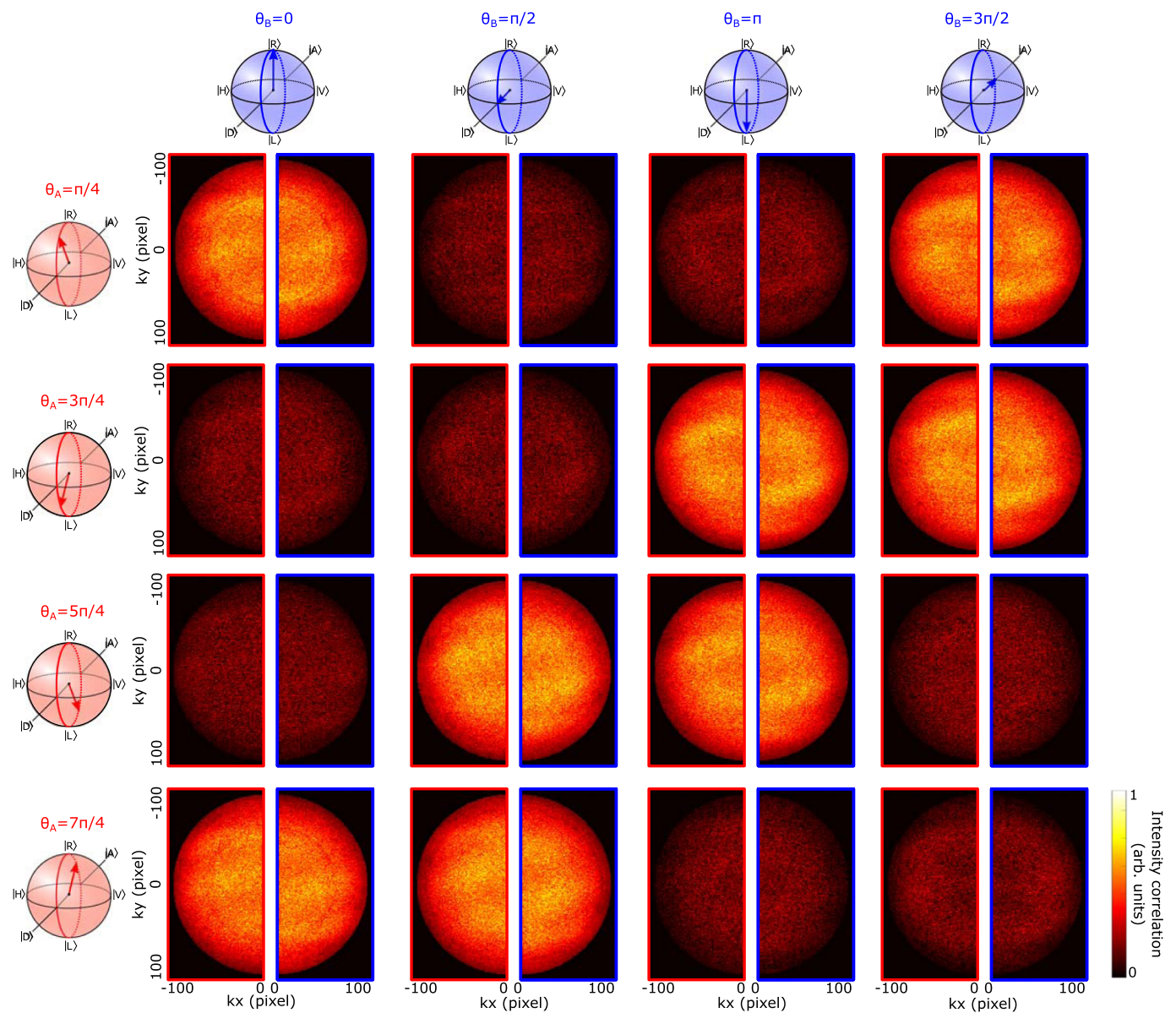
Peer review information *Nature Physics* thanks Alice Meda and the other, anonymous, reviewer(s) for their contribution to the peer review of this work.
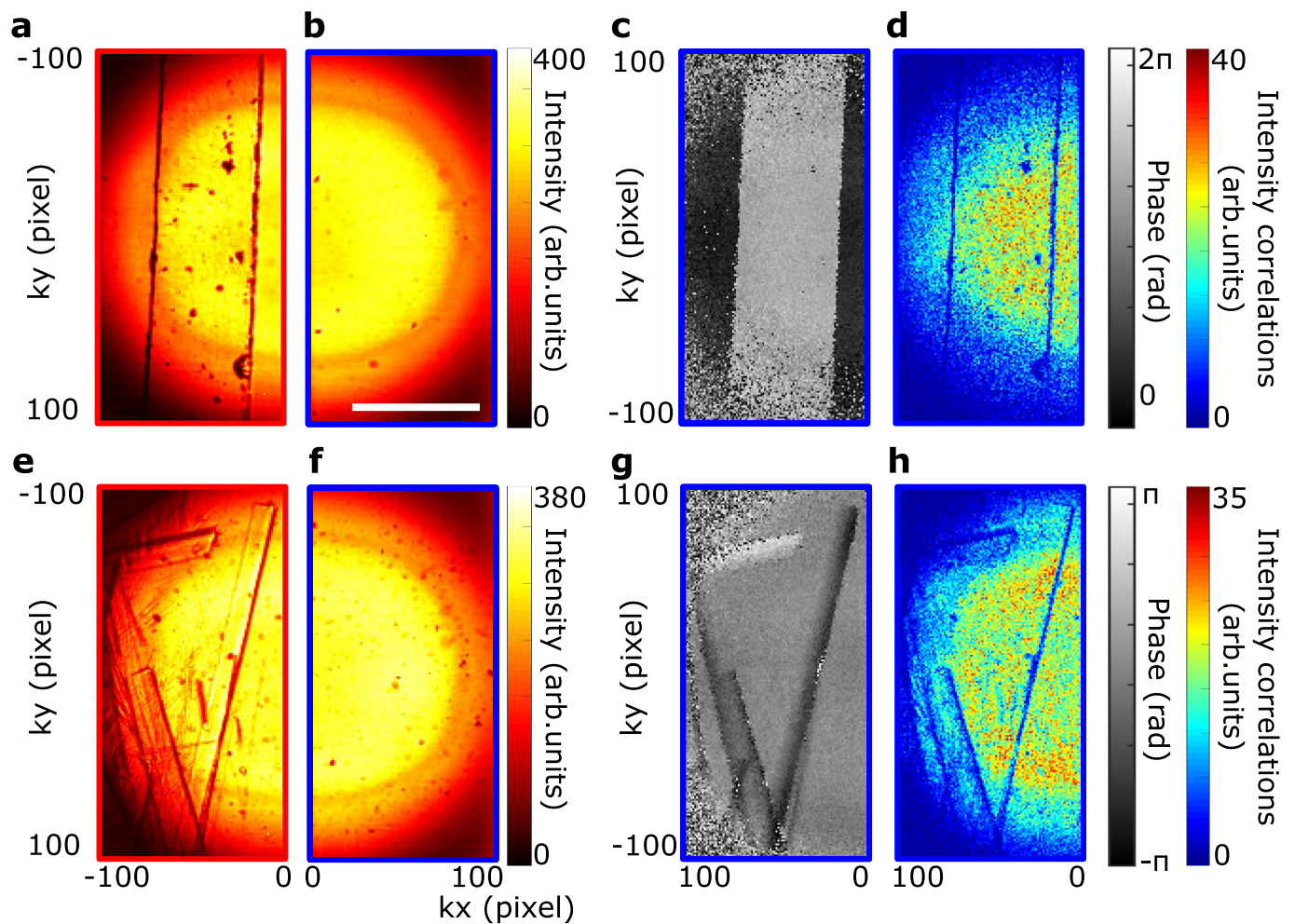
**Reprints and permissions information** is available at www.nature.com/reprints.
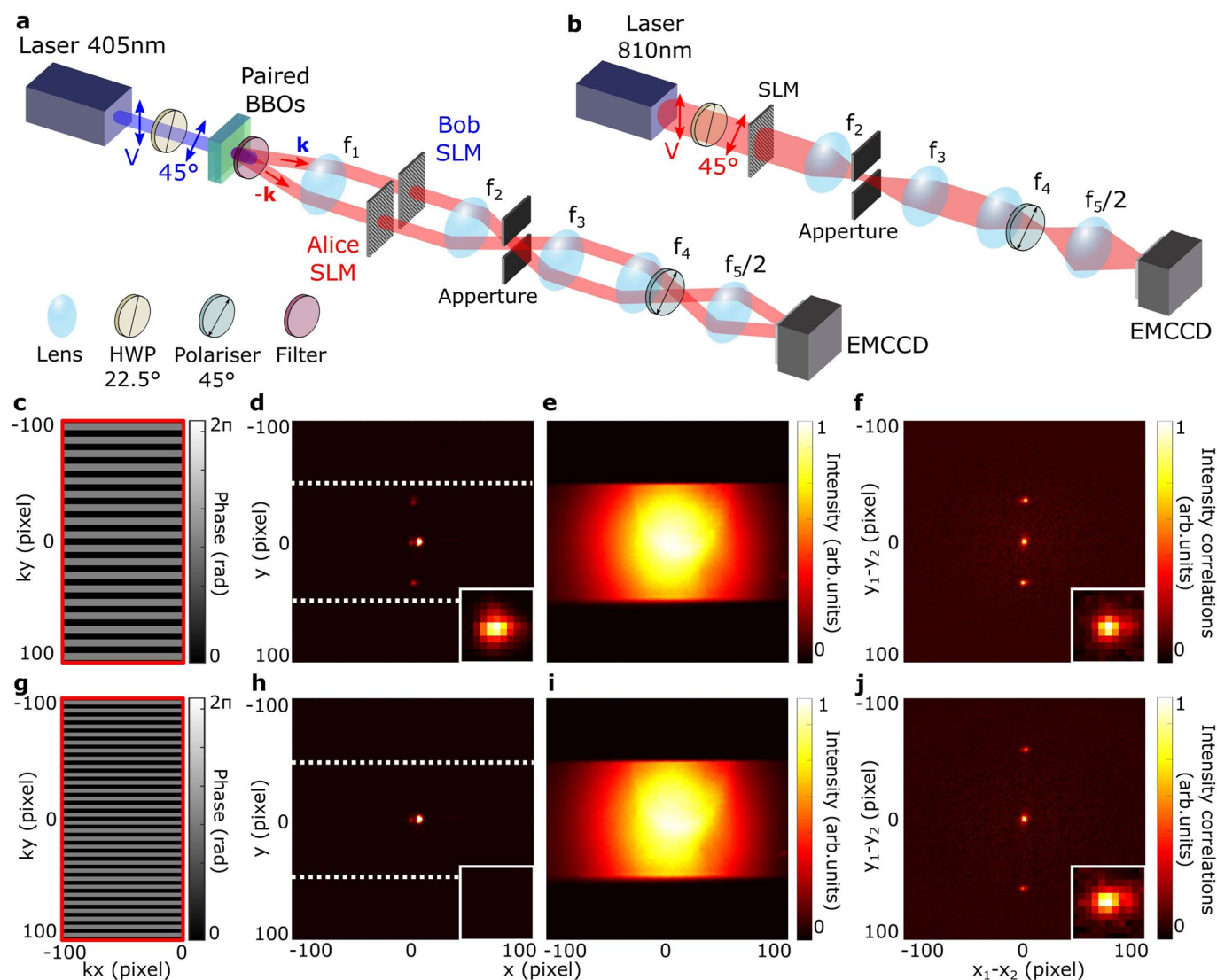
Extended Data Fig. 1 | Resolution enhancement characterisation. a and **b**, Experimental apparatus used for spatial frequency cut-off measurement of the quantum and classical holographic systems, respectively. **c**, 26 pixels period phase grating programmed on the SLM (only Alice SLM in the quantum case). **d**, Intensity image measured with the classical system. Inset is a zoom on the first-order diffraction peak. White dashed lines represent the edges of the aperture. **e**, Intensity image measured in the quantum system. **f**, Projection of the intensity correlation matrix onto the minus-coordinate axis $r_1 - r_2$ that shows three diffraction peaks. Inset is a zoom on the first-order diffraction peak. **g**, 16 pixel-period-phase grating programmed on the SLM. **h**, Intensity image measured with the classical system. First-order diffraction peaks are blocked by the aperture. **i**, Intensity image measured in the quantum system. **j**, Projection of the intensity correlation matrix onto $r_1 - r_2$ that still shows three diffraction peaks.

Extended Data Fig. 2 | Intensity correlation images measured by Alice and Bob for 16 combinations of phase values θ_A and θ_B. Intensity correlation images are shown by pair, with a red outline for Alice and a blue outline for Bob. Each row corresponds to a measurement setting on Alice SLM $\theta_A = \{\pi/4, 3\pi/4, 5\pi/4, 7\pi/4\}$ and each column to a measurement setting of Bob SLM $\theta_B = \{0, \pi/2, \pi, 3\pi/2\}$.

Extended Data Fig. 3 | Quantum holographic imaging of real objects. a, Intensity images measured by Alice showing a piece of transparent scotch tape. **b**, Intensity image measured by Bob. **c**, Phase image reconstructed by Bob with SNR = 14. **d**, Amplitude image reconstructed by Bob from the same set of intensity correlation images by replacing the argument in equation (1) of the article with an absolute value. **e**, Intensity image measured by Alice showing parts of a bird feather. **f**, Intensity image measured by Bob. **g**, Phase image reconstructed by Bob with SNR = 13. **h**, Amplitude image reconstructed by Bob. 10^7 frames were acquired in total for each case. The white scale bar corresponds to 1mm. Phase and amplitude images retrieved by Bob are rotated by 180 degrees for convenience.
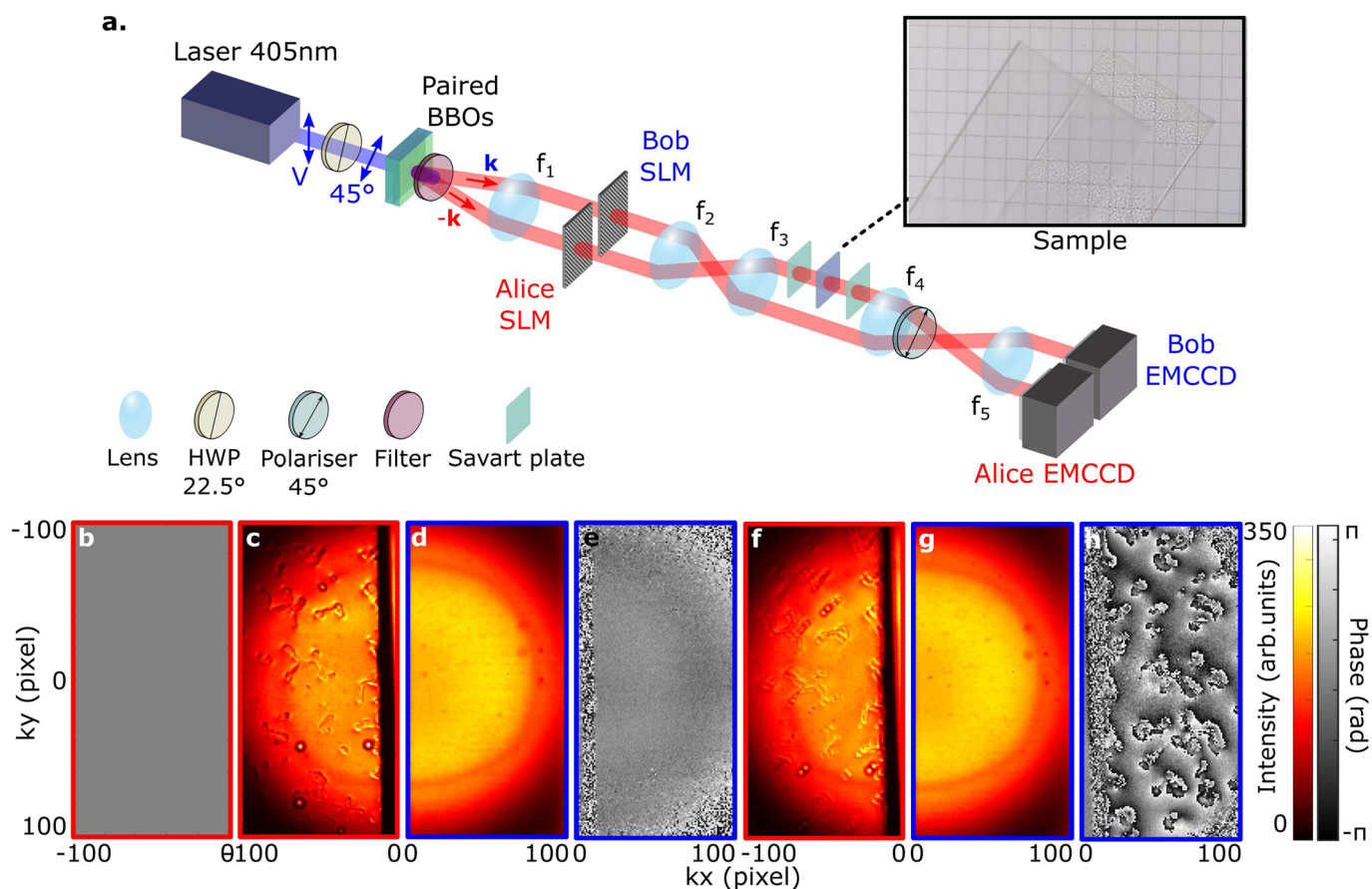
Extended Data Fig. 4 | Quantum holography of non-polarisation sensitive objects. a, Modified quantum holographic set-up to achieve phase imaging of non-polarisation sensitive phase object. The sample is inserted in a conjugate image plane of Alice SLM located between f_3 and f_4. Two Savart plates are inserted on each side of the sample and are slightly tilted. The sample is a microscopic slide covered by a layer of silicone adhesive generated using a spay, that effectively produces a random phase layer. **b,** Flat phase pattern on Alice SLM (not in use in this configuration), **c** and **d,** Intensity images measured by Alice and Bob without the Savart plates. **e,** Phase reconstructed by Bob using the quantum holographic approach without the Savart plates with SNR=17. **f** and **g,** Intensity images measured by Alice and Bob with the Savart plates. **h,** Phase reconstructed by Bob using the quantum holographic approach with the Savart plates with SNR=12. Each phase image was reconstructed from 5.10^6 frames.